Physics in Medicine & Biology

IPEM Institute of Physics and Engineering in Medicine

PAPER • OPEN ACCESS

Dosimetry of microbeam radiotherapy by flexible hydrogenated amorphous silicon detectors

To cite this article: Matthew James Large *et al* 2024 *Phys. Med. Biol.* **69** 155022

View the article online for updates and enhancements.

You may also like

- Synthesis and magnetic heating characteristics of thermoresponsive poly (N-isopropylacrylamide-co-acrylic acid)/nano Fe_3O_4 nanparticles
Thi Thu Trang Mai, Thi Hong Phong Le, Hong Nam Pham et al.
- Controllable nanoscale inverted pyramids for highly efficient quasi-omnidirectional crystalline silicon solar cells
Xu Haiyuan, Zhong Sihua, Zhuang Yufeng et al.
- Simple informative prior distributions for Type A uncertainty evaluation in metrology
Anthony O'Hagan and Maurice Cox

This content was downloaded from IP address 150.217.251.69 on 03/10/2024 at 07:48

IOP Publishing Phys. Med. Biol. 69 (2024) 155022 https://doi.org/10.1088/1361-6560/ad64b5

Physics in Medicine & Biology

IPEM Institute of Physics and Engineering in Medicine

CrossMark

OPEN ACCESS

RECEIVED
12 May 2024

REVISED
26 June 2024

ACCEPTED FOR PUBLICATION
17 July 2024

PUBLISHED
26 July 2024

Original content from this work may be used under the terms of the Creative Commons Attribution 4.0 licence.

Any further distribution of this work must maintain attribution to the author(s) and the title of the work, journal citation and DOI.

PAPER

Dosimetry of microbeam radiotherapy by flexible hydrogenated amorphous silicon detectors

Matthew James Large[1], Keida Kanxheri[2,3], Jessie Posar[1], Saba Aziz[4,5], Aishah Bashiri[1,6], Lucio Calcagnile[4,5], Daniela Calvo[7], Domenico Caputo[8,9], Anna Paola Caricato[4,5], Roberto Catalano[10], Roberto Cirio[7], Giuseppe Antonio Pablo Cirrone[10], Tommaso Croci[3,11], Giacomo Cuttone[10], Gianpiero De Cesare[8,9], Paolo De Remigis[7], Sylvain Dunand[12], Michele Fabi[13,14], Luca Frontini[15], Catia Grimani[13,14], Mariacristina Guarrera[10], Maria Ionica[3], Francesca Lenta[7,16], Valentino Liberali[15,17], Nicola Lovecchio[8,9], Maurizio Martino[4,5], Giuseppe Maruccio[4,5], Giovanni Mazza[7], Mauro Menichelli[3], Anna Grazia Monteduro[4,5], Arianna Morozzi[3], Francesco Moscatelli[3,18], Augusto Nascetti[9,19], Stefania Pallotta[14,20], Daniele Passeri[3,11], Maddalena Pedio[3,18], Giada Petringa[10], Francesca Peverini[2,3], Pisana Placidi[3,11], Gianluca Quarta[4,5], Silvia Rizzato[4,5], Federico Sabbatini[13,14], Leonello Servoli[3], Alberto Stabile[15,17], Jonathan Emanuel Thomet[12], Luca Tosti[3], Mattia Villani[13,14], Richard James Wheadon[7], Nicolas Wyrsch[12], Nicola Zema[3,21], Marco Petasecca[1,*] and Cinzia Talamonti[14,20]

[1] Centre for Medical Radiation Physics, University of Wollongong, Wollongong, Australia
[2] Dip. di Fisica e Geologia dell'Università degli Studi di Perugia, via Pascoli s.n.c., 06123 Perugia, Italy
[3] INFN Sezione di Perugia, via Pascoli s.n.c., 06123 Perugia, Italy
[4] INFN Sezione di Lecce, via per Arnesano, 73100 Lecce, Italy
[5] Department of Mathematics and Physics 'Ennio de Giorgi', University of Salento, via per Arnesano, 73100 Lecce, Italy
[6] Najran University, King Abdulaziz Rd, Najran, Saudi Arabia
[7] INFN Sezione di Torino, Via Pietro Giuria 1, 10125 Torino, Italy
[8] Dipartimento Ingegneria dell'Informazione, Elettronica e Telecomunicazioni, dell'Università degli studi di Roma 'La Sapienza', via Eudossiana 18, 00184 Roma, Italy
[9] INFN Sezione di Roma 1, Piazzale Aldo Moro 2, Roma, Italy
[10] INFN Laboratori Nazionali del Sud, Via S.Sofia 62, 95123 Catania, Italy
[11] Dip. di Ingegneria dell'Università degli studi di Perugia, via G.Duranti, 06125 Perugia, Italy
[12] Ecole Polytechnique Fédérale de Lausanne (EPFL), Photovoltaics and Thin-Film Electronics Laboratory (PV-Lab), Rue de la Maladière 71b, 2000 Neuchâtel, Switzerland
[13] DiSPeA, Università di Urbino Carlo Bo, 61029 Urbino (PU), Italy
[14] INFN Sezione di Firenze, Via Sansone 1, 50019 Sesto Fiorentino, Firenze, Italy
[15] INFN Sezione di Milano, Via Celoria 16, 20133 Milano, Italy
[16] Politecnico di Torino, Corso Duca degli Abruzzi 24, 10129 Torino, Italy
[17] Dipartimento di Fisica dell'Università degli Studi di Milano, via Celoria 16, 20133 Milano, Italy
[18] CNR Istituto Officina dei Materiali (IOM), via Pascoli s.n.c., 06123 Perugia, Italy
[19] Scuola di Ingegneria Aerospaziale Università degli studi di Roma 'La Sapienza', Via Salaria 851/881, 00138 Roma, Italy
[20] Dipartimento di Scienze Biomediche sperimentali e Cliniche 'Mario Serio', University of Florence Viale Morgagni 50, 50134 Firenze (FI), Italy
[21] CNR Istituto struttura della Materia, Via Fosso del Cavaliere 100, Roma, Italy
* Author to whom any correspondence should be addressed.

E-mail: marcop@uow.edu.au

Keywords: microbeam radiation therapy, flexible dosimetry, hydrogenated amorphous silicon, high dose-rate dosimetry, flash photon therapy

Supplementary material for this article is available online

Abstract

Objective. Detectors that can provide accurate dosimetry for microbeam radiation therapy (MRT) must possess intrinsic radiation hardness, a high dynamic range, and a micron-scale spatial resolution. In this work we characterize hydrogenated amorphous silicon detectors for MRT dosimetry, presenting a novel combination of flexible, ultra-thin and radiation-hard features. *Approach.* Two detectors are explored: an n-type/intrinsic/p-type planar diode (NIP) and an NIP with an additional charge selective layer (NIP + CSC). *Results.* The sensitivity of the NIP + CSC detector was greater than the NIP detector for all measurement conditions. At 1 V and 0 kGy under the 3T Cu–Cu synchrotron broadbeam, the NIP + CSC detector sensitivity of (7.76 ± 0.01) pC cGy^{-1} outperformed the NIP detector sensitivity of (3.55 ± 0.23) pC cGy^{-1} by

© 2024 The Author(s). Published on behalf of Institute of Physics and Engineering in Medicine by IOP Publishing Ltd

219%. The energy dependence of both detectors matches closely to the attenuation coefficient ratio of silicon against water. Radiation damage measurements of both detectors out to 40 kGy revealed a higher radiation tolerance in the NIP detector compared to the NIP + CSC (17.2% and 33.5% degradations, respectively). Percentage depth dose profiles matched the PTW microDiamond detector's performance to within ±6% for all beam filtrations except in 3T Al–Al due to energy dependence. The 3T Cu–Cu microbeam field profile was reconstructed and returned microbeam width and peak-to-peak values of (51 ± 1) μm and (405 ± 5) μm, respectively. The peak-to-valley dose ratio was measured as a function of depth and agrees within error to the values obtained with the PTW microDiamond. X-ray beam induced charge mapping of the detector revealed minimal dose perturbations from extra-cameral materials. *Significance.* The detectors are comparable to commercially available dosimeters for quality assurance in MRT. With added benefits of being micron-sized and possessing a flexible water-equivalent substrate, these detectors are attractive candidates for quality assurance, *in-vivo* dosimetry and in-line beam monitoring for MRT and FLASH therapy.

1. Introduction

Microbeam radiation therapy (MRT) is a pre-clinical radiotherapy modality that combines high dose-rate x-rays and spatially fractionated beams for improved treatment efficacy and radiobiological effectiveness (Trappetti *et al* 2021). In order to trigger a radiobiological advantage, MRT adopts spatially fractionated beams with dose-rates that can exceed thousands of Gray (Gy) per second. Microbeams are obtained by passive slit collimators with apertures of 50–100 μm and centre-to-centre distance between slits in the order of 0.4–1 mm. In this paper we report on FLASH MRT which refers to the combination of the FLASH effect with spatial fractionation of ultra-high dose-rate (UHDR) photon beams (Bouchet *et al* 2013, Wilson *et al* 2020). In order to maintain sub-millimetre precision of the UHDR spatially fractionated microbeams, minimal beam divergence must be guaranteed. For these reasons, FLASH MRT is currently confined to synchrotron facilities (Blattmann *et al* 2005). The peak-to-valley dose ratio (PVDR) of the microbeam field is a pivotal dosimetric quantity for MRT, as a high contrast between peaks and valleys is an essential requirement to facilitate the tissue-sparing effect (Dilmanian *et al* 2007, Romanelli and Bravin 2011, Engels *et al* 2023). An in-depth discussion of the advancements in FLASH MRT is provided by Engels *et al* (2020). More recently, the generation of microbeams using conventional x-ray tubes has also been explored in pre-clinical contexts (Bartzsch *et al* 2016, Steel *et al* 2021, Treibel *et al* 2021). As this paper only concerns dosimeters designed for FLASH MRT, it is hereafter referred to as simply MRT.

Dosimeters for MRT must overcome a number of challenges to be able to accurately perform quality assurance. Firstly, they must possess a large dynamic range to accurately reconstruct the dose delivered in both the peaks and valleys of the MRT field. For example, film-based quality assurance for MRT typically employs two different sensitivity Gafchromic films; a low dose film (EBT3 film with 0.1–20 Gy range) for mapping of the valley dose and a high dose film (HD-V2 film with 10–1000 Gy range) for mapping of the peaks (Ocadiz *et al* 2019). The dosimeter should also possess a sensitivity (or charge-to-dose calibration factor) that is dose-rate independent to avoid the need for complex dose-rate and energy dependent correction factors. Furthermore, the spatially fractionated MRT field requires detectors to possess a spatial resolution in the order of microns to reconstruct the profiles and avoid volume averaging effects. A tissue-equivalent response, whilst not strictly required, is highly desirable to avoid the need for complex energy-dependent calibration factors when performing dosimetry. Lastly, they should possess a high intrinsic radiation hardness to withstand constant exposure to the high dose-rate treatment beams of MRT. The currently employed standard for reference dosimetry in MRT is the PTW microDiamond (TN60019) detector (Livingstone *et al* 2018, Davis *et al* 2019, Brace *et al* 2020). The microDiamond is a Schottky diode detector fabricated on a cylindrical synthetic diamond sensitive volume with a radius of 1.1 mm and 1 μm thickness (Livingstone *et al* 2016, Brace *et al* 2020). As the linear dimensions of the microDiamond detector closely approximate those of the detectors of this work, any volume averaging effects encountered during experimental measurements will be comparable between both the PTW microDiamond and the hydrogenated amorphous silicon (a-Si:H) detectors of this work. One major limitation of the microDiamond detector is the time consuming and complex alignment process required to make use of the devices high spatial resolution capabilities (Davis *et al* 2019). Moreover, the use of synthetic diamond requires precise and costly manufacturing techniques that are only practical for small, rigid sensitive volumes.

Hydrogenated amorphous silicon (a-Si:H) is an attractive candidate for high dose-rate x-ray dosimetry. The deposition of a-Si:H is typically performed via plasma enhanced chemical vapour deposition (PECVD), meaning that it can be fabricated over large areas at a relatively low cost, and onto a variety of substrates including flexible materials (Shah *et al* 1992). The authors have published a feasibility study on a-Si:H detector technologies for MRT dosimetry (Large *et al* 2023). These detectors employed large pixel sizes of 4×4 mm^2, intrinsic a-Si:H layer thickness of up to 6.2 μm deposited on a thick glass substrate. These first generation detectors displayed superior radiation hardness and accurate broad beam dosimetry of the UHDR synchrotron beam. However, a number of limitations were identified. Firstly, the large sensitive volumes resulted in volume averaging effects for both broad beam and MRT dosimetry. The size of the pixels further limited the dynamic range in which the detector could operate, restricting its dosimetry capabilities to only the low dose-rate modalities of the synchrotron facility. The thick (1–3 mm) glass substrates were susceptible to heating effects from the extreme dose-rates of the MRT beams, causing an increase in the detector noise and variations of the response during irradiations. Most notably, the use of silver-based conductive paints to facilitate electrical readout of the detectors was identified to cause inaccuracies in the dosimetric performance of these devices. X-ray beam induced charge (XBIC) mapping of the sensor revealed that approximately 90% of the detector response was caused by fluorescence from the silver glue adopted for the electrical contacts. Finally, a dose-rate dependence was observed for a pristine (non-irradiated) a-Si:H device. The combination of dose-rate dependence, limited dynamic range, and dose-enhancement effects from silver contacts resulted in these first generation a-Si:H MRT dosimeters to provide poor PVDR response.

The goal of the INFN project 'HASPIDE' is to overcome these limitations and develop a-Si:H detectors specifically for x-ray dosimetry (Menichelli *et al* 2024). In this work, we characterise a-Si:H diode structures deposited directly onto a flexible, water-equivalent substrate and packaged by use of low atomic number materials, for applications in MRT dosimetry. These flexible detectors possess a novel architecture described as a hybrid planar barrier diode design. Furthermore, these detectors have been fabricated with a reduced pixel size and improved electrical contact technologies. This improved contacting method uses thinner wires and a carbon-based conductive paint, rather than the silver-based paints previously identified to cause dose-enhancement which resulted in inaccuracies when evaluating the PVDR of the synchrotron microbeams. A comprehensive assessment of this new generation of flexible a-Si:H dosimeters for MRT is provided, detailing their performance for quality assurance measurements and dosimetry in both broad beam and microbeam modalities. Further investigations into the impact of the a-Si:H detector architectures and packaging are also performed including radiation damage, stem effect and charge collection pixel mapping of the detector. The combined flexibility, radiation hardness and scalability of the a-Si:H detectors in this work present clear avenues for improvement over the current commercially available dosimetry solutions for MRT.

2. Methodology

2.1. Experimental facility and beamline filtrations

The Australian Synchrotron, operated by the Australian Nuclear Science and Technology Organisation, is a 3 GeV synchrotron radiation facility with a nominal storage ring current of 200 mA. All experimental measurements were performed ex-vacuo in Hutch 2B of the imaging and medical beamline (IMBL). This experimental hutch is located 32 m downstream of the superconducting multipole wiggler magnet. The intensity and energy spectrum of the IMBL's extracted x-ray beam can be tuned by varying the magnetic field strength of the wiggler as well as through the use of in-vacuo filter paddles (Stevenson *et al* 2017, Dipuglia *et al* 2019). The metallic foils of the in-vacuo filter paddles 4 and 5 include aluminium (Al), copper (Cu) and a molybdenum–aluminium alloy (Mo). All other filter paddles remained in the standard configuration (Hausermann *et al* 2010). In this study, four different beam filtrations were utilized under a 3T wiggler field strength; Al–Al, Cu–Al, Cu–Cu and Mo–Mo. See section 2.1.2 and table 1 for the corresponding weighted average energy and dose-rate of each filter combination.

2.1.1. Reference conditions for dosimetry

Reference dosimetry conditions for broad-beam exposure describes detectors at a depth of 2 cm in a water-equivalent plastic (solid water) phantom (10×10 cm^2 cross-sectional area) and with 8 cm of solid water as backscatter. The incident synchrotron x-ray beam is shaped to produce a 20×20 mm^2 field using a conformal mask, with the beam height restricted to 0.5 mm through the use of a beam defining aperture (BDA). The detector and phantom are translated vertically through the 20×20 mm^2 field via a motorized stage known as the 'DynMRT' stage.

Table 1. Reference dosimetry of the IMBL's 3T broad beam taken with the PTW 31 022 PinPoint IC at reference dosimetry conditions and at a vertical scan speed of 10 mm s^{-1}. Results are taken as the average of 3 scans and the error calculated as one standard deviation.

Beam filtration	Weighted average energy (keV)[a]	Delivered dose (Gy)[b]	Dose-rate (Gy s^{-1})
Mo–Mo	124	1.207 ± 0.045	22.12 ± 0.82
Cu–Cu	95.1	9.78 ± 0.36	179.1 ± 6.6
Cu–Al	82.9	25.08 ± 0.93	460 ± 17
Al–Al	55.0	219.8 ± 8.1	4027 ± 150

[a] Energies taken from Livingstone *et al* (2018).

[b] Doses calculated at reference conditions and with temperature, pressure and polarization corrections applied.

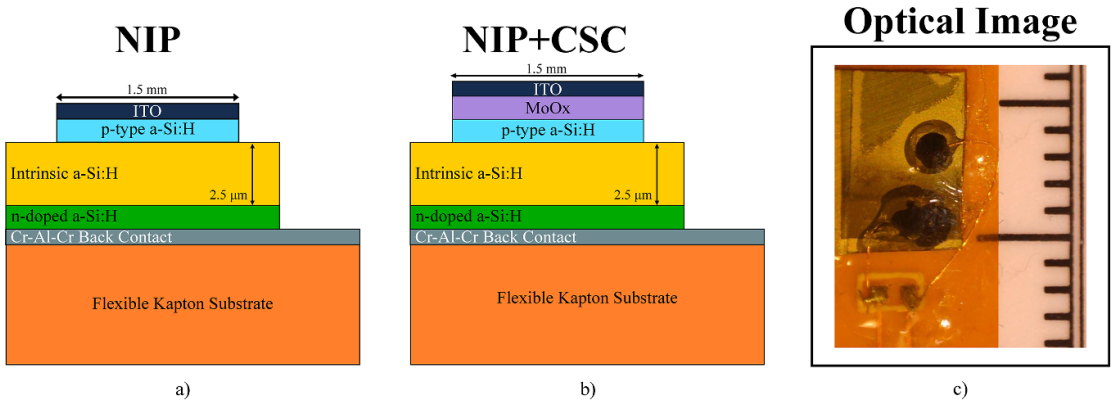

Figure 1. Detector schematic for a-Si:H devices with (a) NIP and (b) NIP + CSC architectures. (c) An optical microscope image of the detector mounted on a Kapton probe for electrical readout. The scale next to the device has millimetre increments.

2.1.2. IMBL beam calibration dosimetry

Reference dosimetry was performed using the PTW 31 022 3D PinPoint ionization chamber (IC) under reference dosimetry conditions. For each of the four beam filter combinations, the IC was scanned vertically through the beam at a speed of 10 mm s^{-1}. The absolute doses recorded by the PTW IC were corrected for temperature, pressure and polarization. Three scans were performed for each filtration, with the dose received taken as the average and the uncertainty taken as the standard deviation. Table 1 summarizes the delivered dose and dose-rate measured with the IC under reference conditions for each filter combination.

2.2. a-Si:H detector descriptions

The detectors are described as planar barrier diodes fabricated directly on a flexible 25 μm polyimide (DuPont™ Kapton® HN) substrate and were manufactured at the PV-Lab of École Polytechnique Fédérale de Lausanne, Neuchâtel, Switzerland. Throughout this work, two different detector architectures are investigated. Both designs possess a 2.5 μm intrinsic a-Si:H layer, pixels with a sensitive area of 1.5 × 1.5 mm^2, and a Cr–Al–Cr back electrical contact deposited via metal sputtering.

The n-type/intrinsic/p-type planar diode (NIP) detector possesses an n–i–p stack diode design (from bottom to top: n-type, intrinsic, and p-type semiconductor layers) whereby the a-Si:H layers are deposited by PECVD at a temperature of 200 °C. The intrinsic a-Si:H layer has a nominal thickness of 2.5 μm and is deposited using a combination of Silane (SiH_4) and hydrogen gas. The n-doped and p-doped a-Si:H layers are fabricated by introducing PH_3/H_2 and trimethylborane (TMB)/H_2 gases, respectively, during the PECVD process. These doped layers are on the order of tens of nanometres in thickness. The top contact is formed via sputtering of approximately 28 nm of indium-tin-oxide (ITO) directly on top of the p-doped a-Si:H layer. To define the desired sensitive pixel area, a final SF6 + O_2 dry-etching is performed to remove the p-doped layer and isolate individual pixels (figure 1(a)).

The NIP + CSC detector possesses a core structure that is identical to that of the NIP detectors, with the addition of a charge selective top-contact (CSC). Specifically, a 20 nm molybdenum oxide layer (MoO_x) is sputter coated over the p-doped a-Si:H layer of the n–i–p stack, before finally depositing the top ITO layer and again performing the dry etching process (figure 1(b)).

The a-Si:H detectors were mounted onto custom-designed printed circuit pigtails manufactured with Kapton (35 cm long) to interface with an electrometer designed by the Centre for Medical radiation Physics at the University of Wollongong, Australia (Fuduli *et al* 2014). Electrical contact between the detector and the

pads of the readout tail was made using thin (50 μm ∅) copper wires and a carbon-based conductive paint (MG Chemicals 838AR), encapsulated with a layer of two-part epoxy (figure 1(c)).

2.3. Experimental methods

All measurements were performed under reference dosimetry conditions unless otherwise specified. When a bias is specified, the value reported is the magnitude of the reverse bias that was applied; i.e. a cited detector bias of 1 V refers to a +1 V applied to the back contact (Cr–Al–Cr) of the detector.

Broad beam dosimetry measurements and the XBIC collection map were performed with the detector in a face-on orientation. When situated face on, the incident synchrotron beam strikes the detector pixel at normal incidence. For MRT measurements (profiling, PVDR) where superior spatial resolution is required, devices are positioned 'edge-on'. Placing the detector in an edge-on orientation exposes the side profile of the detector to the oncoming beam, whereby the thickness of the intrinsic layer (i.e. 2.5 μm) determines the maximum spatial resolution of the detector (see figure S1 in supplementary information).

2.3.1. Stem effect estimations

To quantify the contribution of the stem effect to the recorded detector response, the NIP + CSC detector assembled on a readout tail was scanned vertically through the 3T Cu–Al synchrotron broad beam at a speed of 10 mm s^{-1}. The detector was then removed and the measurements repeated with a bare Kapton readout tail (i.e. no a-Si:H detector mounted). Stem effect measurements were performed with an applied bias of 1 V.

2.3.2. Linearity and calibration factors

The dose linearity of the detectors was investigated for all four beam filter configurations and outlined in table 1. To modulate the dose delivered, the vertical scan speed of the DynMRT stage was varied. For each beam filtration, irradiations were performed with vertical scan speeds of 5 mm s^{-1}, 10 mm s^{-1} and 20 mm s^{-1}. The absorbed dose delivered for each scan speed was calculated from reference scans using the PTW IC (table 1). For each dose/scan speed, three irradiations were performed with the average response recorded (after baseline subtraction). The errors in the calibration factors (table 2) represent one standard deviation.

Linearity measurements were performed for applied biases of 0 V and 1 V for both detectors (NIP and NIP + CSC). Additionally, measurements were taken for each detector when pristine (0 kGy) and pre-irradiated (40 kGy). Details of the pre-irradiation procedure are provided in section 2.3.4. The resulting dose linearity figures are provided in the supplementary information (figures S2 and S3). By applying a linear fit to the linearity data, the detectors dose calibration factors were calculated for each beam filtration as a function of bias and lifetime dose. The dose calibration factors of the NIP + CSC detector are given in table 2. The NIP detectors calibration factors can be found in table S1 of the supplementary information.

2.3.3. Energy dependence

As shown in table 1, changing the beam filtration also changes the energy profile of the incident x-ray beam. Hence, the energy dependence in the detector calibration factors was also assessed. By plotting the obtained detector calibration factors against the average weighted energy for each beam filtration, the energy dependence was obtained for energies from 55 to 124 keV.

2.3.4. Radiation damage

The Al–Al filtration of the IMBL was selected as it possesses the highest instantaneous dose rate for the 3 T wiggler field. For the NIP device, irradiations were performed under reference dosimetry conditions (2 cm depth, 8 cm backscatter), while for the NIP + CSC device irradiations were performed at a 5 cm depth due to the NIP + CSC detectors increased sensitivity resulting in saturation of the electrometer at the standard 2 cm depth. Both detectors were operated at 0 V during irradiations. Each irradiation consisted of a 10 mm s^{-1} vertical scan resulting in a dose of ∼220 Gy/scan for the NIP detector (2 cm depth) and ∼118 Gy/scan for the NIP + CSC detector (5 cm depth), respectively. After each scan, the integral charge was calculated with the average baseline subtracted. Irradiations were repeated until the intended pre-irradiation dose of 40 kGy was delivered to both detectors. The detector responses were normalized to their initial responses (i.e. 0 kGy prior lifetime dose).

2.3.5. Percentage depth dose (PDD)

Detectors were placed at depths ranging from 5 mm to 60 mm in solid water, with 3 vertical DynMRT scans (10 mm s^{-1}) performed at each depth. The resulting PDD curves present the average response at each depth normalized against the response under reference dosimetry conditions (i.e. a depth of 2 cm). The PDD response of the commercially available PTW microDiamond (TN 60019) detector has been included as a

benchmark. The responses of the microDiamond detector are taken from Livingstone *et al* (2018) for the 3T Mo–Mo beam, and from Posar *et al* (2021) for the remaining filtrations (i.e. Cu–Cu, Cu–Al and Al–Al).

2.3.6. Microbeam field profile and field factor

All microbeam irradiations were performed with the beam in 3T Cu–Cu modality. The tungsten multi-slit collimator (MSC) produces microbeams with a nominal full-width half-maximum (FWHM) of 50 μm and a peak to peak separation of 400 μm. High spatial resolution mapping of the microbeam field profile was performed the detector situated in edge-on mode (figure S1) and biased at 1 V. An intrinsic scan was performed by moving the detector laterally through the centre of the microbeam field at a speed of 0.5 mm s^{-1}. By retrieving the detector response with a 5 ms signal integration time, the microbeam profile was reconstructed with an effective spatial resolution of 2.5 μm (figure 6(a)). From this, the field factor is calculated by comparing the intrinsic scan of the broad beam field with the microbeam field, and taking the ratio of the average response observed at the microbeam peaks with the average broad beam response.

However, the intrinsic scan method provides only the spatial distribution in beam intensity. To measure the dose profile of the microbeam field, a methodology known as step-and-shoot (SnS) must be employed. For SnS the detector is positioned edge-on and is advanced horizontally in discrete increments, with a full vertical DynMRT irradiation performed at each increment. The dose profile of the three central microbeams was performed via SnS using the NIP + CSC detector biased at 1 V (post 40 kGy). For accurate mapping, 5 μm steps were used to reconstruct the microbeam peaks and 20 μm steps taken in the valleys. After each step, three vertical scans at 10 mm s^{-1} were performed, with the average dose per irradiation calculated.

2.3.7. PVDR as a function of depth

The PVDR was measured via SnS over the central microbeams, using the same procedure described in section 2.3.6. Using the pre-irradiated (40 kGy TID) NIP + CSC detector in edge-on mode, SnS scans were performed at depths between 10 mm and 50 mm in solid water. At each depth, the PVDR was calculated by taking the ratio of the average peak dose to the average valley dose across the central microbeams. The average peak dose was calculated from the mean maximum dose of the central five microbeams, and the average valley dose calculated from the mean dose in the middle 100 μm of the four surrounding valleys. The PVDR as a function of depth was recorded for 0 V and 1 V detector biases. Measurements were also repeated using the PTW microDiamond detector as a reference, with the microDiamond detector also situated in an edge-on orientation to take advantage of its 1 μm thickness. A previously published PVDR vs Depth response of the PTW microDiamond at IMBL was also included for validation of the methodology (Livingstone *et al* 2018).

2.3.8. X-ray beam induced charge (XBIC)

To create a charge collection map of the a-Si:H detector, a single microbeam with dimensions 50 × 50 μm was isolated using the MRT beam collimators. With the detector face-on with respect to the beam, a rasterised scan process is performed, scanning horizontally across the face of the detector before incrementing its position vertically with respect to the beam in 50 μm steps. The charge collected by the detector is recorded as a function of relative position to the beam, with a signal integration time of 5 ms.

3. Results

After preliminary measurements of the NIP and NIP + CSC detectors, it was observed that the NIP + CSC detector design consistently possessed a higher sensitivity and a lower, more stable leakage current (particularly under external bias). For this reason, the NIP + CSC detector was chosen as the primary detector to perform broad beam and MRT dosimetry. Thus, the following results section primarily displays the results of the NIP + CSC detector. The response of the NIP detector is available in the supplementary information document that accompanies this publication and may be discussed in this document where there are notable comparisons to be made.

3.1. Stem effect

The results of the stem effect measurements for a 3T Cu–Al broad beam are presented in figure 2. The contribution of the stem effect for Cu–Cu and Al–Al filtrations was also investigated and are included in the supplementary information (figure S2). Both traces in figure 2 display the response of the detector during a DynMRT scan (vertical) for a 20 mm height field at a speed of 10 mm s^{-1}. The response obtained from the detector when the beam is directly incident on the pixel is the large central peak. The peripheral non-zero response is caused by the beam interacting with the phantom and the resulting electron scattering interacting with the detector. This direct irradiation of the pixel produces a peak with approximately 50 times higher

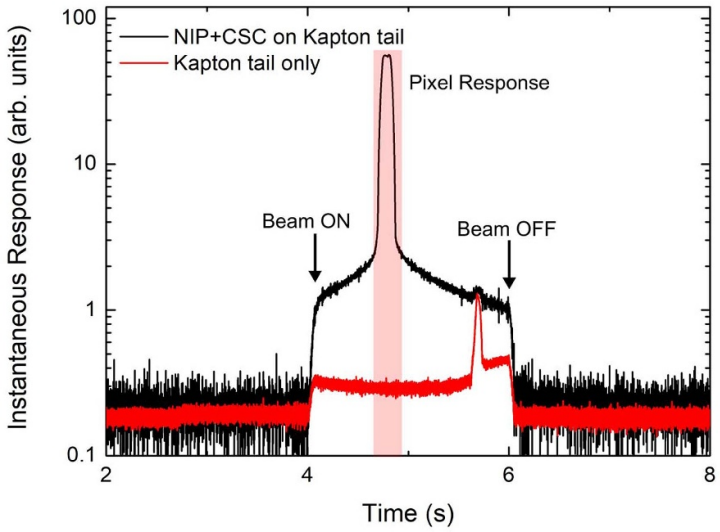

Figure 2. Contribution of the stem effect, with the NIP + CSC detector response (black) and the induced signal from a bare Kapton readout tail (red) overlayed. Results are presented for a 1 V external bias applied through the readout tail and irradiated by a 10 mm s^{-1} vertical scan through the 3T Cu–Al synchrotron broad beam under reference conditions.

amplitude than the signal from the scattered radiation within the water-equivalent plastic phantom. The FWHM of the peak is approximately 1.5 s, corresponding to an edge of the pixel which is approximately 1.5 mm.

Comparing the NIP + CSC response to that of the Kapton tail only (red trace in figure 2), the induced signal via the stem effect is comparable in magnitude to the electronic noise of the fully assembled detector during irradiation. The most notable effect of the Kapton PCB tail comes from the direct irradiation of the solder pads by the synchrotron beam (see figure 1(c)). Direct irradiation of these pads results in the peak in the instantaneous response trace of the Kapton tail. This was identified by examining the temporal instant at which the peak occurred and the beams position across the Kapton tail during the data acquisition. The presence of an induced signal from these pads is also evident in the NIP + CSC trace by the small bump that aligns with the peak (black trace in figure 2). A quantitative analysis of the signals reveals that the stem effect contributes to the integral signal from the detector by 3.6%.

3.2. Linearity and calibration factors

Both the NIP and NIP + CSC detectors returned excellent dose linearities under all pre-irradiation, bias and beam filtration conditions. This is supported by the calculated values of the linear regression coefficient, which lies between 0.9997 and 1.0000 for all measurements. The dose calibration factors are calculated from the slopes of the dose linearity plots (figures S3 and S4). The highest sensitivity recorded was for the NIP + CSC detector at (10.4 ± 0.03) pC cGy^{-1} irradiated with the 3T Cu–Al broad beam under a 1 V bias and with 0 kGy pre-irradiation. A systematic decrease in sensitivity is observed following a 40 kGy pre-irradiation of the detectors. For the NIP + CSC detector, the sensitivity after 40 kGy decreases by between 29% (Cu–Al beam, 1 V bias) and 47% (Mo–Mo beam, 0 V bias). For 0 kGy pre-irradiation, the NIP + CSC detector exhibits an increase in sensitivity of approximately 180% from the application of a 1 V external bias. This sensitivity increase due to the application of external bias becomes more pronounced after 40 kGy at 234%. Similar trends are observed in the NIP detector.

Table 2 presents the calibration factors for the NIP + CSC detector (in pC cGy^{-1}) for all measurement conditions investigated. Note that due to saturation of the electrometer, measurements under a 1 V bias were not collected for the Al–Al beam modality. As the NIP + CSC variant is the primary detector used for further broad beam and MRT dosimetry measurements, the calibration factor results of the NIP detector are instead included in the supplementary material (table S1).

3.3. Energy dependence

Figure 3 presents the energy dependence results of the NIP + CSC detector under the different bias and pre-irradiation conditions. The results in figure 3 are normalized against the 3T Cu–Cu detector response, with the error bars calculated by propagating the uncertainties of table 2. The energy dependence of the NIP detector is available in the supplemental (figure S5) and matches closely the energy dependence observed here in the NIP + CSC detector. Results suggest the energy dependence of the detectors is largely unaffected by the

Table 2. NIP + CSC detector calibration factors obtained for multiple 3T broad beam filtrations. All calibration factors presented are calculated from the performed dose linearity measurements. Calibration factors under 1 V bias were unable to be recorded for the NIP + CSC detector due to saturation of the electrometer.

		Sensitivity under 3T beam filtrations (pC cGy^{-1})			
Pre-irradiation	Detector bias	Mo–Mo	Cu–Cu	Cu–Al	Al–Al
0 kGy	0 V	2.96 ± 0.01	4.57 ± 0.01	4.51 ± 0.02	8.64 ± 0.01
	1 V	5.50 ± 0.10	7.76 ± 0.01	10.4 ± 0.03	—
40 kGy	0 V	1.38 ± 0.01	2.33 ± 0.01	3.35 ± 0.01	5.92 ± 0.01
	1 V	3.71 ± 0.12	4.94 ± 0.01	7.39 ± 0.01	—

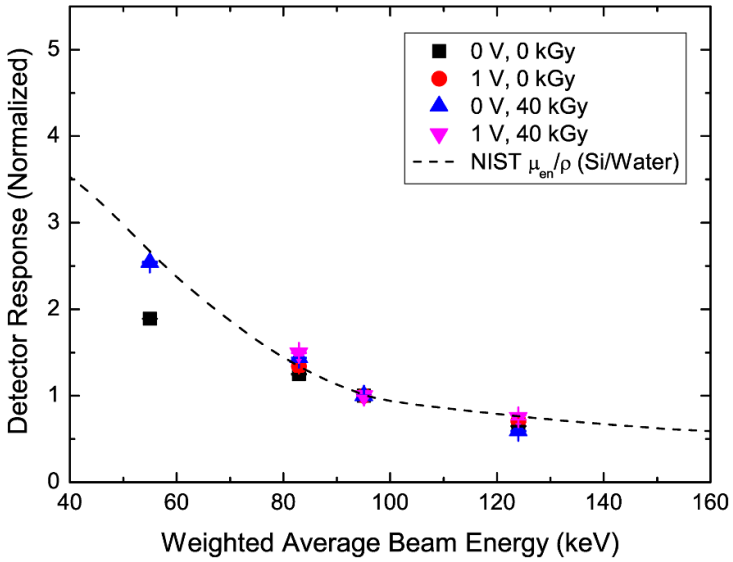

Figure 3. Energy dependence of the NIP + CSC detector under different bias (0 V or 1 V) and pre-irradiation (0 kGy or 40 kGy) conditions. Results are the average of 3 repeated exposures and are normalized against the response to the 3T Cu–Cu beam (95 keV weighted average energy). Error bars represent the standard deviation between repeated measurements and are contained within the marker sizes. The ratio of mass-energy absorption coefficient (μ_{en}/ρ) for silicon over water, taken from the NIST database (Hubbell and Seltzer 2004), is plotted for comparison (dashed line).

application of external bias or pre-irradiation, with the energy dependence closely approximating the ratio of mass energy absorption coefficients (μ_{en}/ρ) of silicon to water extracted from the NIST x-ray attenuation database (Hubbell and Seltzer 2004). The correlation of the NIP + CSC detector's energy dependence and the μ_{en}/ρ ratio of silicon to water, combined with the similarity in energy dependence of the NIP detector, confirms a-Si:H active layer dominates the energy dependence. Furthermore, this result demonstrates the detectors energy dependence is not affected by the extra-cameral materials such as the carbon-based electrical contacts, Kapton substrate or the epoxy used for encapsulation. For detector measurements under 1 V bias, energy dependence at the 55 keV weighted average beam energy could not be obtained due to saturation of the electrometer by the beams associated high dose-rate at this energy (see table 1).

3.4. Radiation damage

Radiation damage measurements were performed on both NIP and NIP + CSC detector types during the pre-irradiation phase of the detectors with a total dose up to 40 kGy. This maximum dose was selected to ensure significant radiation induced damage whilst keeping increases in detector leakage currents to a minimum to maintain functionality of the detector. Figure 4 shows the change in integral response of the detectors as a function of increasing cumulative lifetime dose.

The NIP + CSC detector displays a response degradation of 33.5% after an exposure of 40 kGy TID. The degradation rate slows with increasing dose in both detectors. For the NIP + CSC detector, a 10% response degradation occurs after 4.7 kGy, yet an additional 11 kGy is required to reach a 20% total reduction in response. The NIP detector response displays a similar radiation-induced damage effect to the NIP + CSC detector but at a much slower rate. After the 40 kGy pre-irradiation, the NIP detector response degrades by approximately half as much as the NIP + CSC detector variant, returning a 17.2% decrease in comparison to the detector's pristine sensitivity. The presence of multiple interfaces in the NIP + CSC detector, such as the

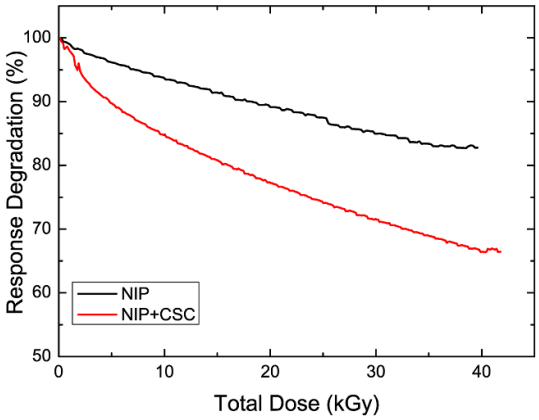

Figure 4. Radiation damage for NIP (black) and NIP + CSC (red) a-Si:H detectors up to a total lifetime dose of 40 kGy. Variation of the detector response is given as integral detector response for a given total dose as a percentage of the detectors initial (0 kGy TID) response. Irradiations were performed using the 3T Al–Al broad beam of the IMBL, with detectors under a 0 V bias during irradiations and measurements.

charge selective contact layer between the ITO and the doped a-Si layer, increases the probability of trapped charges which reduces the charge extraction efficiency of the sensor. This issue is mitigated in the NIP architecture where there is no additional CSC layering. Despite this issue, leakage current in NIP + CSC samples is still lower than in NIP samples following this substantial irradiation. Under 0 V bias, both detectors do not display any substantial increases in leakage current following 40 kGy of pre-irradiation. Under 1 V bias, the NIP detectors leakage current increased by 97% from (1.13 ± 0.11) pC to (2.23 ± 0.21) pC after 40 kGy. The associated errors in the average leakage current values represent one standard deviation. Comparatively, the leakage current of the NIP + CSC detector under 1 V external bias was recorded as (0.208 ± 0.087) pC for 0 kGy prior dose versus (0.235 ± 0.092) pC after 40 kGy, corresponding to a leakage current increase of 13%. Therefore, the high built-in potential barrier created by the CSC layer is still effective even after 40 kGy of TID.

3.5. Percentage depth dose (PDD)

Figures 5(a)–(c) present the PDD curves for the NIP + CSC detector irradiated in 3T modality with beam filtrations Mo–Mo, Cu–Cu, and Cu–Al, respectively. The subplots below the PDD curves in figure 5 display the percentage difference between the a-Si:H and the microDiamond responses. The results display the variation in the detector's response as a function of depth in water-equivalent plastic (also known as solid water). Results are compared directly against the PDD response of the PTW microDiamond detector. For 3T Mo–Mo, the PTW microDiamond data is taken from Livingstone *et al* (2018). For the 3T Cu–Cu and 3T Cu–Al modalities, the PTW microDiamond data is extracted from Posar *et al* (2021).

The PDD response of the NIP + CSC detector shows a close agreement to the PTW microDiamond for all the filtrations. As displayed in the subfigure of figures 5(a)–(c), the variation between the two detectors in all cases is contained to within ±6%. Results are presented for different bias configurations of the NIP + CSC detector for the Mo–Mo and Cu–Al filtrations, with no appreciable effects of the applied bias observed in the resulting PDD response. Furthermore, the effect of pre-irradiation is investigated for the Cu–Cu beam filtration. Similarly to an applied bias, it is inconclusive as to whether pre-irradiation of the detector provides any additional benefits to the PDD response. The largest discrepancy between the NIP + CSC detector and the PTW microDiamond in figures 5(a)–(c) is a 5.25% overresponse at a 40 mm depth in the 3T Mo–Mo field, with the NIP + CSC detector pre-irradiated and with a 1 V external bias applied.

For the highest dose-rate modality in 3T Al–Al, the NIP + CSC detector's sensitivity resulted in the saturation of the readout electronics for majority of the shallow depths in the PDD profile. The NIP detector with its slightly lower sensitivity was therefore utilized for reconstructing the PDD for this filtration. Although it possesses a different architecture, its PDD response is assumed to be essentially identical. This is supported by the comparison of the two detector types provided in the supplementary information, where the NIP detectors PDD profile shows similar agreements against the PTW microDiamond (figures S6(a)–(c)) and a close agreement against the NIP + CSC detector for 3T Cu–Cu (figure S6(d)).

The PDD profile obtained with the NIP a-Si:H detector in Al–Al filtration, displays a significant difference in response compared to the PTW microDiamond and is indicative of the expected response also from the NIP + CSC detector. At depths shallower than the 20 mm, the a-Si:H detector over responds by up to 24.8%, while its response underestimates the dose at deeper positions by −15%. This behaviour is a

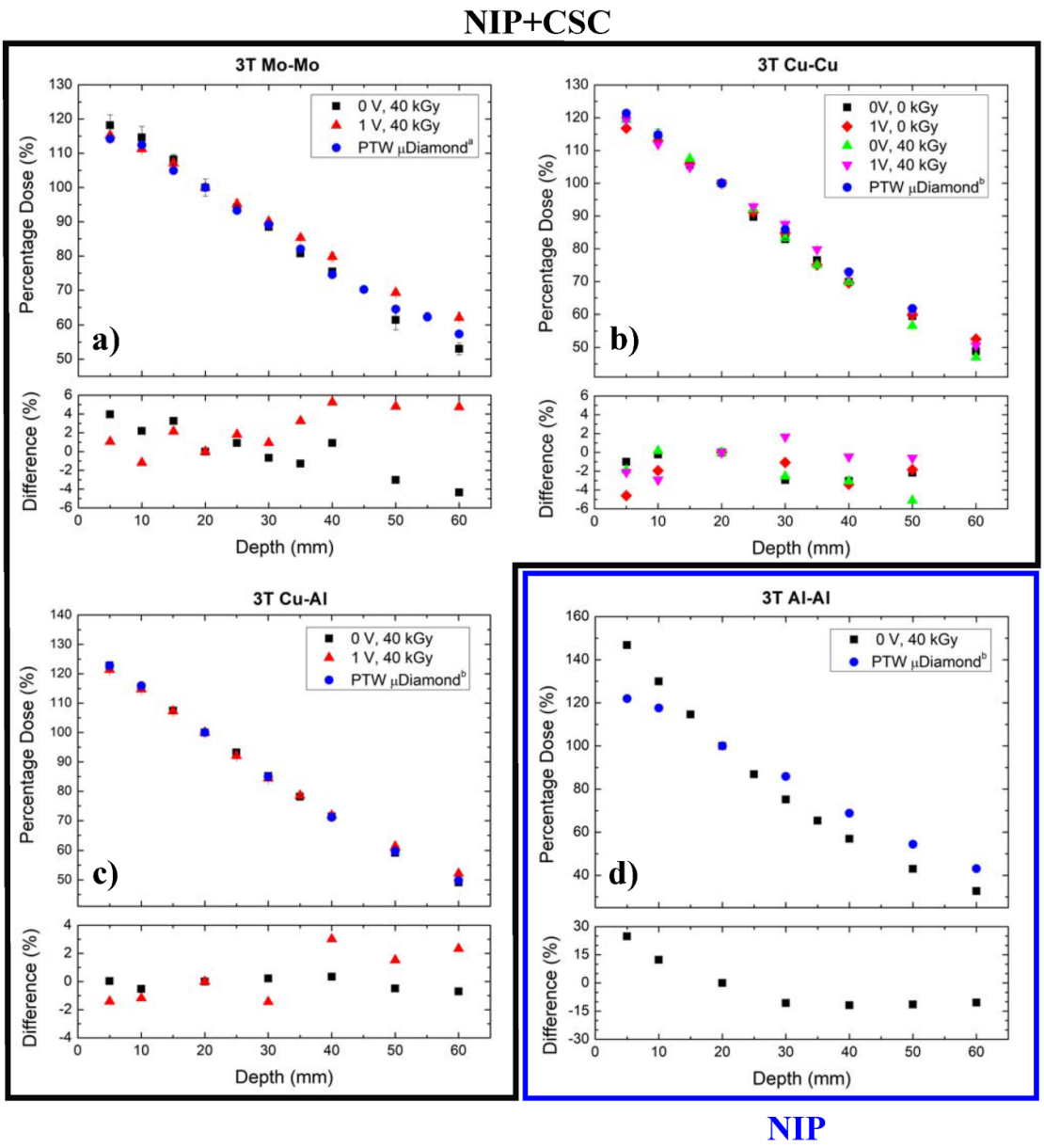

Figure 5. PDD curves for the NIP + CSC a-Si:H detector for (a) Mo–Mo, (b) Cu–Cu, and (c) Cu–Al beam filtrations (3T wiggler fields). (d) PDD response of the NIP a-Si:H detector irradiated by the 3T Al–Al beam. Detector responses are presented for various bias and pre-irradiation conditions and represent an average of 3 repeated exposures at each data point. The error bars represent the standard deviation and are contained within the markers. The subplots depict the percentage difference between the a-Si:H detector with respect to the PTW microDiamond data extracted from literature (a—Livingstone *et al* 2018 , b—Posar *et al* 2021). Error bars are propagated from the PDD curves but are again contained within the size of the markers.

consequence of the energy dependence of the a-Si:H (figure 3) and the variation of the spectrum as a function of depth in water in 3T Al–Al filtration. The spectrum from Al–Al filtration hardens (increases average beam energy) with depth, and the detector sensitivity varies substantially in this same energy range due to the photoelectric effect becoming dominant (figure 3). The softer (lower average energy) spectrum at the surface produces an over-response in the detector while the harder spectrum at depth of 30–50 mm produces an under-response in respect to the calibration depth of 20 mm.

3.6. Microbeam field profile and field factor

The reconstructed microbeam profile is given in figure 6 for the 3T Cu–Cu MRT field. The field was reconstructed with the NIP + CSC a-Si:H detector (pre-irradiated) in an edge-on orientation and biased at 1 V. Figure 6(a) shows the lateral beam profiles of the synchrotron broad beam and microbeams, mapped via intrinsic scan. By comparing the broad beam and microbeam profiles, a field factor can be inferred due to the introduction of the MSC. The field factor is calculated by taking the average height of the microbeam peaks and dividing this by the average signal height of the broad beam. The resulting field factor for the 3T

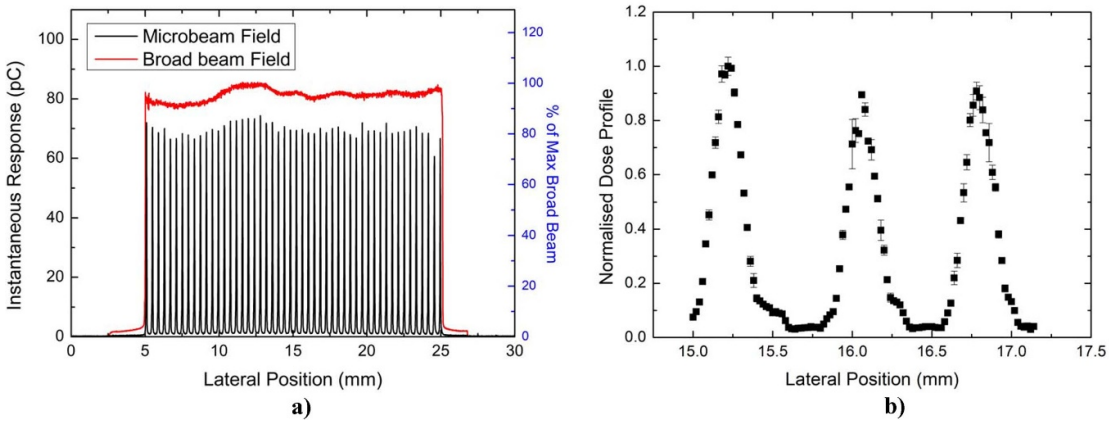

Figure 6. (a) Intrinsic scan of the microbeam profile (black) encompassed in the profile of the 20 × 20 mm^2 broad beam. (b) Step-and-shoot dose profiling of the central microbeams. Profiles in both figures were recorded by the pre-irradiated NIP + CSC detector (40 kGy lifetime dose) under 1 V bias and in an edge-on orientation. The error bars in figure 6(b) represent the standard deviation in the dose recorded from the three irradiations delivered at each lateral position.

Cu–Cu synchrotron beam was calculated as (80 ± 4)% and agrees with similar values previously obtained within the relevant literature (Bräuer-Krisch *et al* 2015).

Figure 6(a) further demonstrates that variations observed in the heights of the microbeam peaks are due to variations across the broad beam profile. These variations likely arise from imperfections in the BDA which collimates the synchrotron beam vertically. This was confirmed by reversing the direction of the intrinsic scan and observing features that initially appeared towards the beginning of the scan now appeared towards the end, and vice versa.

The resulting dose profile of the central microbeams, normalised against the maximum local dose, is given in figure 6(b). From the SnS profile of the central microbeams in figure 6(b), the FWHM and the peak-to-peak spacing of the synchrotron microbeams were calculated as (51.0 ± 1.0) μm and (405 ± 2) μm, respectively. These values are in close agreement with the expected microbeam field dimensions at a distance of 1 m downstream from the MSC which possesses nominal 50 μm slit widths and a 400 μm centre-to-centre slit spacing. Also evident in figure 6(b) are the existence of some slight distortion to the right of each microbeam peak, attributed to scattering produced by the extra-cameral materials (i.e. epoxy, carbon-paint and wires) which is then collected by the sensitive volume.

3.7. PVDR vs depth

The central microbeams were profiled by the NIP + CSC detector at depths from 10 to 60 mm in water-equivalent plastic via SnS. From these profiles, the PVDR was calculated at each depth for the detector under 0 V and 1 V external biases. Figure 7 shows the resulting depth profile of the PVDR from the synchrotron microbeams, calculated from the average peak and valley doses over the central microbeams for each depth, with the error bars representing one standard deviation over three repetitions. An identical methodology was employed to performed PVDR vs depth measurements with a PTW microDiamond detector. This was benchmarked against existing PTW microDiamond data of the PVDR vs depth from literature (Livingstone *et al* 2018).

A close agreement between the NIP + CSC and PTW microDiamond response is once again observed. Larger error bars are present for 0 V measurements, particularly for shallower depths where the recorded PVDR value has an uncertainty of between ±3 and ±5. At shallower depths, the valley dose rate is particularly low. Therefore, a combination of decreased sensitivity of the sensor when unbiased and low dose rate is the likely cause of higher uncertainties in determining the valley dose. This can be mitigated by the application of external bias and is supported by the 1 V detector response which contains error bars of less than ±1 for all depths except 10 mm. Whilst the application of bias improves the precision of individual dose measurements, the average values of the PVDR as a function of depth remain substantially independent from bias conditions, considering that the small variations recorded are within the error bars of the experimental data. Furthermore, a variation in PVDRs obtained by the microDiamond detector, both from literature and from this study, is also observed and is comparable to the variation observed between the a-Si:H devices. The PVDR values for all depths agree (within experimental error) to the values measured using the PTW microDiamond and demonstrate a significant improvement against the previous generation of a-Si:H detectors previously published, where a factor of approximately 2.8 was observed between the two datasets

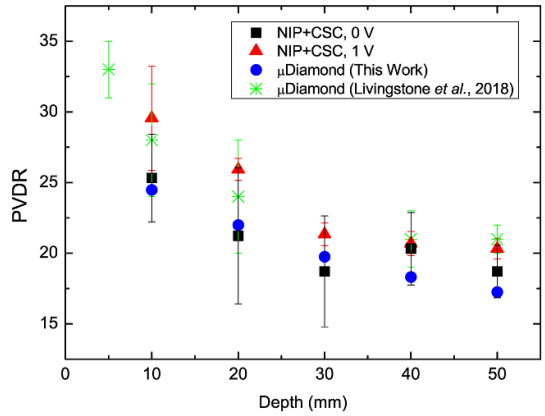

Figure 7. Recorded PVDR values as a function of water-equivalent depth. PVDR values are calculated as the ratio of the average dose received in the microbeam peaks to the average dose of the valleys. Error bars represent one standard deviation.

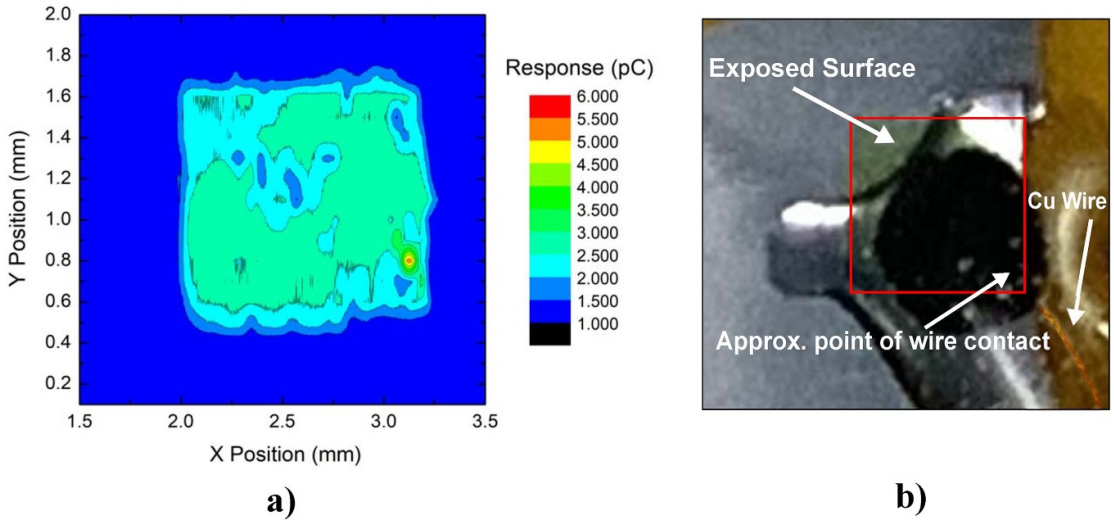

Figure 8. (a) XBIC collection efficiency map of a NIP + CSC detector. (b) Optical microscope image of the detector pixel mapped via XBIC for direct comparison. An outline of the pixel is overlayed (red) as the image contrast and resolution makes identifying the pixel position difficult.

(Large *et al* 2023). In this work, a maximum discrepancy by a factor of 1.22 is observed at 10 mm between the 1 V detector data and the microDiamond data recorded during this work.

3.8. XBIC detector map

There are two regions of interest in the XBIC map in figure 8(a) that correspond to physical features of the pixel and the electrical contact. The first is the localized area of increased charge collection at the bottom right of the pixel. This is attributed to the collimated beam directly irradiating the 50 μm diameter copper wire, inducing a current in the wire by stem effect. This is also confirmed by the red trace in the data reported in figure 2. The second feature is the area of lower charge collection in the top-left of the XBIC pixel map. This feature corresponds to the segment of the detector pixel that is not covered with two-part epoxy, as seen in the optical image of the pixel in figure 8(b). The lower quantity of charge collected by the section of pixel without epoxy implies the presence of some response-enhancement from the epoxy, theorized to be due to a fluorescence optical light generated by the organic polymers used in the glue. Previous work with such materials has confirmed that epoxy plastics emits a faint blue light when irradiated by high flux x-ray photons (Posar *et al* 2021). It is evident from figure 8(a) that the carbon-based conductive paint used to connect electrically the ITO at the surface of the a-Si:H substrate and the copper wire produces no dose-enhancement. This confirms the authors' hypothesis that the extreme dose-enhancements previously encountered when using a silver-based conductive paint (Large *et al* 2023) could be removed by substituting its use for a conductive paint with a lower effective atomic number.

4. Discussion

The work presents the crucial advancement of radiation monitoring in MRT with a flexible, radiation-hard, high-spatial resolution a-Si:H detector. The a-Si:H detectors presented in this work represent a significant improvement over the previous generation published in Large *et al* (2023). Most notably, the use of a carbon-based conductive paint provides a sound electrical contact with the polyimide (Kapton) tail and electronic readout without perturbing the induced signal from the synchrotron beam. The use of silver-based conductive paint in synchrotron beams has been previously reported to cause localized areas of increased charge collection attributed to the generation of secondary electrons and K-shell soft x-rays (approx. 22 keV) (Large *et al* 2023). This dose-enhancement effect from silver-based contacts was responsible for a seven-fold increase in localized charge collection versus direct detection of electrons by a-Si:H. As shown in figure 8(a), the carbon-based paint produces no parasitic signal. There is, however, some increased signal (approximately +12%) induced by the coverage of the a-Si:H pixel with epoxy, contributing to an additional 0.2–0.5 pC of instantaneous response. This effect was also observed in previous detector generations (Large *et al* 2023). While this contribution has little impact on linearity and depth dose in broad beam dosimetry, a complete coverage of the pixel with epoxy would ensure a uniform response and may result in more accurate dosimetry of the microbeams when the detector is used in edge-on orientation. Future work might also explore alternative, more rigorous electrical contacting methods such as Anisotropic Conductive Film tap bonding or flip-chip assembling.

Another improvement over previous generations of the amorphous sensors is the deposition of the sensitive layer directly on polyimide, replacing the standard substrate used for this technology which is sapphire or glass (Pietrikova *et al* 2016). Kapton is a material that has a high degree of superficial roughness that affects the quality of the Al–Cr–Al metalization and the uniformity of film deposited over it. Although this is detrimental for the overall performance, the recorded sensitivities of the a-Si:H detectors developed for this work and deposited on kapton are comparable to the detectors fabricated on glass substrates (Large *et al* 2023). The NIP + CSC contact combination has helped to compensate for the quality of the amorphous substrate and represents an important innovation in respect to previous technologies. The NIP + CSC samples provided sensitivities on the order of pC cGy^{-1}, with the highest sensitivity recorded as (10.4 ± 0.03) pC cGy^{-1} for pristine and 1 V biased operation in a 3T Cu–Al field (see table 2). Normalized by the 1.5×1.5 mm^2 sensitive area of the detector pixel, this corresponds to a (4.62 ± 0.01) pC cGy^{-1} mm^{-2} that is equivalent to NIP a-Si:H detector structures on glass substrate and under a 1 V external bias, recorded at 4T Mo–Mo field.

Despite the risk of detrimental effects on the charge collection, the use of Kapton as a substrate is extremely important in achieving the desired dosimetric qualities of the a-Si:H detectors for use in x-ray modalities such as microbeam RT. The x-ray absorption and scattering generated by the Kapton substrate is similar to that of water (Wu *et al* 2020) and is extremely thin ($\sim$25 μm) allowing a good heat dissipation during high dose-rate irradiations. Kapton's water-equivalent x-ray scattering and absorption properties is beneficial in providing a more water-equivalent detector response when performing dosimetry. This is particularly evident in the excellent PDD response of the NIP + CSC detector for the Mo–Mo, Cu–Cu and Cu–Al beam spectra. For Mo–Mo and Cu–Cu filtrations, the variation in the recorded PDD profile is well within $\pm$6% to the profiles recorded with the PTW microDiamond (Livingstone *et al* 2018, Posar *et al* 2021). This margin between a-Si:H and the microDiamond is further reduced to within $\pm$4% for the 3T Cu–Al broad beam field. As the PTW microDiamond's PDD response is assumed to be that of a water-equivalent detector, a close agreement infers a sufficient water-equivalent response from the a-Si:H detector in predicting the broad beam dose as a function of depth.

The exception to the excellent agreement in PDD profiles between a-Si:H and the PTW microDiamond is for the 3T Al–Al beam modality. In this beam mode, the average weighted energy is lowest (55 keV) and the dose-rate is the highest (see table 1). Using a depth of 2 cm in solid water as calibration point, a systematic under response of the a-Si:H with respect to the PTW microDiamond profile is observed with increasing depth. Similarly, an over response is recorded for all depths shallower than the reference depth. These large variations of up to 24.8% are due to the a-Si:H's recorded energy dependence and the shifting of the beams energy spectrum that occurs at changing depths. For shallow depths, the energy spectrum of the beam is softer than under reference dosimetry conditions (i.e. 20 mm depth). The energy spectrum of the beam hardens with increasing depth. Referring to the recorded energy dependence of the NIP + CSC detector's response, the regions of under and over response in the Al–Al PDD profile can be easily predicted. For the higher average-energy beam filtrations, the beam's shifting energy spectra with depth results in a less-pronounced effect that is essentially negligible, as the energy dependence in the detector's sensitivity varies by less than 25% for energies between 80 keV and 125 keV (see figure 3). In theory, this effect can be mitigated by determining the effective weighted average energy of the Al–Al beam at each depth and applying

the corresponding energy correction factor extrapolated from figure 3. However, this limitation of the detector has little practical impact as the Al–Al beam modality of the Australian Synchrotron's IMBL is rarely implemented in MRT pre-clinical or biological studies due to the heightened risk of increased skin dose/toxicity due to the low average energy and extreme dose-rate.

The Kapton substrate's flexibility, combined with the thin a-Si:H detector layers, renders the entire detector structure fully flexible. This pairing of Kapton's flexibility and x-ray water equivalency allows for a-Si:H detectors fabricated on Kapton to be a viable candidate for future *in-vivo* and in-beam dosimetry solutions for MRT (Large *et al* 2024). However, the use of a Kapton substrate is not without drawbacks. Regarding radiation hardness, the sensitivity of both detector architypes degraded after TID of 40 kGy. As shown in figure 4, the NIP + CSC detector sensitivity degraded by 33.5% after 40 kGy, and the NIP detector to a lesser extent with a 17.2% degradation after 40 kGy. Comparing to the previous generation of a-Si:H detectors fabricated on thick glass substrates, a decrease in sensitivity of only 9% after 50 kGy was recorded. Furthermore, a TID of over 280 kGy was required for the a-Si:H detectors on glass before a 30% degradation was observed. Kapton creates issues during the fabrication process: the repeated heating and cooling of the Kapton substrate during metal evaporation and PECVD steps of the detector fabrication caused bubbling and lifting of the substrate due to thermal expansion and contraction effects, respectively. This further contributed to the poor planarity and material interface between the detector layers and the substrate. It is these interface defects between the detector layers and the flexible substrate which are attributed to the decreased radiation tolerance compared the glass substrate detectors of Large *et al* (2023). Methods are available to control these effects, such as surface treatments and etching of the Kapton substrate before deposition of device layers. These will be explored in future work.

The energy dependence of the NIP + CSC detector's dose calibration factor is summarized in figure 3. This data is extrapolated using the recorded detector sensitivities from table 2 and the weighted average energy of the different synchrotron beam spectra as reported in table 1. The resulting energy dependence of the detector appears to be independent of the pre-irradiation or bias conditions imposed, suggesting that a single set of energy-corrections can be applied independently of the applied bias or prior lifetime dose. More importantly, this energy dependence closely follows the energy profile of the mass-energy attenuation coefficient (μ_{en}/ρ) ratio of silicon to water. The μ_{en}/ρ values for silicon and water as a function of energy are extracted from the NIST online x-ray database (Hubbell and Seltzer 2004). The close agreement between the energy dependence of the NIP + CSC detector's sensitivity and the μ_{en}/ρ of Si/H_2O confirms that the a-Si:H material layers are the primary contributor to the energy dependence. This is beneficial as the energy dependence can be accurately predicted from the silicon to water μ_{en}/ρ ratio. Furthermore, this result confirms that the extra-cameral materials such as the carbon-based electrical contacts, the Kapton substrate and the two-part epoxy glue bear no significant effects on the energy dependence of the detector.

The determination of the FWHM and peak-to-peak spacing of the microbeams using the NIP + CSC detector returned values of (51 ± 1) μm and (405 ± 2) μm, respectively (figure 6(b)). These measurements are within experimental error of the expected values for a sensor at 2 cm depth in solid water and 1 m downstream from the collimator. Accurate profiling of the microbeam and broad beam fields also allowed for a precise determination of the field factor that is experienced when switching from broad beam to microbeam modality (figure 6(a)). This is an important quantity used to accurately predict the doses expected in the microbeam peaks based off any broad beam dosimetry performed prior to pre-clinical experiments on cells or small animals. The field factor was measured as (80 ± 4)% with the NIP + CSC detector for the 3T Cu–Cu field, matching the expected field factor from literature (Pellicioli *et al* 2021). The field factor itself arises from the extreme collimation of the broad beam by the MSC, resulting in a reduction of the maximum intensity of the beam due to the strong lateral disequilibrium of the secondary charge particles and partial superposition of the penumbras of the beam.

Finally, the use of carbon-based conductive paint and a flexible, x-ray water equivalent substrate resulted in an accurate determination of the PVDR of the 3T Cu–Cu microbeam field as a function of depth, as seen in figure 7. In the previous generation of a-Si:H detectors, the thick glass substrates caused a filtering of the spectrum in the valleys of the microbeam profile, resulting in a valley dose overresponse. Consequently, a large under-estimation of the PVDR by a factor of approximately 2.8x was observed (see Large *et al* 2023). For the pre-irradiated NIP + CSC detector investigated in this work, both biased and un-biased measurements returned accurate depth profiling of the microbeam fields PVDR. The recorded PVDR values were benchmarked against measurements obtained using the PTW microDiamond detector both experimentally and from literature (Livingstone *et al* 2018). With the application of external bias, the PVDR values measured by the NIP + CSC a-Si:H detector at depths between 20 mm and 60 mm contained errors of less than ± 1 (figure 7).

5. Conclusions

An extensive assessment of the dosimetric performance of a-Si:H detectors for quality assurance in MRT was performed. Significant advances in the accuracy of MRT dosimetry using a-Si:H detectors were achieved thanks to improvements in the design, fabrication, and electrical contacting of the detector. In particular, the recorded PVDR values at various depths in water-equivalent plastic have improved drastically in comparison to previous generations of a-Si:H detectors with larger sensitive volumes and silver-based electrical contacts. Therefore, the a-Si:H detectors used in this study show great potential in performing accurate dosimetry in challenging high dose-rate radiation therapies such as photon FLASH and MRT.

Data availability statement

All data that support the findings of this study are included within the article (and any supplementary information files).

Acknowledgments

This work was conducted under the INFN HASPIDE project. M J Large is supported by the Australian Government Research Training Program (AGRTP) scholarship and the Australian Institute of Nuclear Science (AINSE) Post-Graduate Research Award (PGRA). PhD of F Peverini was supported by Italian PON funding according to DM 1061 DEL 10.8.2021. Experiments at the Australian Synchrotron's IMBL were conducted under awarded beamtime AS231/IMBL/19343. This work is further supported by the Istituto Nazionale di Fisica Nucleare Scientific Committee (3D-SIAM and HASPIDE projects) and the Swiss National Science Foundation.

ORCID iDs

Matthew James Large https://orcid.org/0000-0002-6866-1943
Aishah Bashiri https://orcid.org/0000-0003-3273-9435
Giuseppe Antonio Pablo Cirrone https://orcid.org/0000-0001-5733-9281
Michele Fabi https://orcid.org/0000-0002-2464-1369
Luca Frontini https://orcid.org/0000-0002-1137-8629
Giuseppe Maruccio https://orcid.org/0000-0001-7669-0253
Stefania Pallotta https://orcid.org/0000-0003-4123-7971
Maddalena Pedio https://orcid.org/0000-0002-3305-4318
Silvia Rizzato https://orcid.org/0000-0002-3908-4796
Jonathan Emanuel Thomet https://orcid.org/0000-0002-7528-7312
Nicolas Wyrsch https://orcid.org/0000-0002-4588-0166
Nicola Zema https://orcid.org/0000-0003-2705-6146
Marco Petasecca https://orcid.org/0000-0001-5958-7457
Cinzia Talamonti https://orcid.org/0000-0003-2955-6451

References

Bartzsch S, Cummings C, Eismann S and Oelfke U 2016 A preclinical microbeam facility with a conventional x-ray tube *Med. Phys.* **43** 6301–8

Blattmann H *et al* 2005 Applications of synchrotron x-rays to radiotherapy *Nucl. Instrum. Methods Phys. Res.* A **548** 17–22

Bouchet A *et al* 2013 Synchrotron microbeam radiation therapy induces hypoxia in intracerebral gliosarcoma but not in the normal brain *Radiother. Oncol.* **108** 143–8

Brace O J, Alhujaili S F, Paino J R, Butler D J, Wilkinson D, Oborn B M, Rosenfeld A B, Lerch M L F, Petasecca M and Davis J A 2020 Evaluation of the PTW microDiamond in edge-on orientation for dosimetry in small fields *J. Appl. Clin. Med. Phys.* **21** 278–88

Bräuer-Krisch E, Adam J F, Alagoz E, Bartzsch S, Crosbie J, DeWagter C and Stugu B 2015 Medical physics aspects of the synchrotron radiation therapies: microbeam radiation therapy (MRT) and synchrotron stereotactic radiotherapy (SSRT) *Phys. Med.* **31** 568–83

Davis J A, Petasecca M, Cullen A, Paino J R, Archer J, Rosenfeld A B and Lerch M L F 2019 X-Tream dosimetry of synchrotron radiation with the PTW microDiamond *J. Instrum.* **14** P10037

Dilmanian F A, Qu Y, Feinendegen L E, Peña L A, Bacarian T, Henn F A, Kalef-Ezra J, Liu S, Zhong Z and McDonald J W 2007 Tissue-sparing effect of x-ray microplanar beams particularly in the CNS: is a bystander effect involved? *Exp. Hematol.* **35** 69–77

Dipuglia A, Cameron M, Davis J A, Cornelius I M, Stevenson A W, Rosenfeld A B, Petasecca M, Corde S, Guatelli S and Lerch M L 2019 Validation of a Monte Carlo simulation for microbeam radiation therapy on the imaging and medical beamline at the Australian Synchrotron *Sci. Rep.* **9** 17696

Engels E *et al* 2020 Toward personalized synchrotron microbeam radiation therapy *Sci. Rep.* **10** 8833

Engels E *et al* 2023 Modulating synchrotron microbeam radiation therapy doses for preclinical brain cancer *Radiation* **3** 183–202

Fuduli I, Porumb C, Espinoza A A, Aldosari A H, Carolan M, Lerch M L, Metcalfe P, Rosenfeld A B and Petasecca M 2014 A comparative analysis of multichannel data acquisition systems for quality assurance in external beam radiation therapy *J. Instrum.* **9** T06003
Hausermann D, Hall C, Maksimenko A and Campbell C 2010 The imaging and medical beam line at the Australian Synchrotron *AIP Conf. Proc.* **1266** 3–9
Hubbell J H and Seltzer S M 2004 x-ray Mass Attenuation Coefficients: NIST Standard Reference Database 126 (National Institute of Standards and Technology) (available at: www.nist.gov/pml/x-ray-mass-attenuation-coefficients)
Large M J, Bashiri A, Dookie Y, McNamara J, Antognini L, Aziz S and Petasecca M 2024 Characterization of a flexible a-Si:H detector for in vivo dosimetry in therapeutic x-ray beams *Med. Phys.* **51** 4489–503
Large M J, Bizzarri M, Calcagnile L, Caprai M, Caricato A P, Catalano R and Petasecca M 2023 Hydrogenated amorphous silicon high flux x-ray detectors for synchrotron microbeam radiation therapy *Phys. Med. Biol.* **68** 135010
Livingstone J, Stevenson A W, Butler D J, Häusermann D and Adam J F 2016 Characterization of a synthetic single crystal diamond detector for dosimetry in spatially fractionated synchrotron x-ray fields *Med. Phys.* **43** 4283–93
Livingstone J, Stevenson A W, Häusermann D and Adam J F 2018 Experimental optimisation of the x-ray energy in microbeam radiation therapy *Phys. Med.* **45** 156–61
Menichelli M, Antognini L, Aziz S, Bashiri A, Bizzarri M, Calcagnile L and Zema N 2024 Characterization of hydrogenated amorphous silicon sensors on polyimide flexible substrate *IEEE Sens. J.* **24** 12466–71
Ocadiz A *et al* 2019 Film dosimetry studies for patient specific quality assurance in microbeam radiation therapy *Phys. Med.* **65** 227–37
Pellicioli P, Donzelli M, Davis J A, Esteve F, Hugtenburg R, Guatelli S, Petasecca M, Lerch M L F, Brauer-Krisch E and Krisch M 2021 Study of the x-ray radiation interaction with a multislit collimator for the creation of microbeams in radiation therapy *J. Synchrotron Radiat.* **28** 392–403
Pietrikova A, Lukacs P, Jakubeczyova D, Ballokova B, Potencki J, Tomaszewski G, Pekarek J, Prikrylova K and Fides M 2016 Surface analysis of polymeric substrates used for inkjet printing technology *Circuit World* **42** 9–16
Posar J A *et al* 2021 Towards high spatial resolution tissue-equivalent dosimetry for microbeam radiation therapy using organic semiconductors *J. Synchrotron Radiat.* **28** 1444–54
Romanelli P and Bravin A 2011 Synchrotron-generated microbeam radiosurgery: a novel experimental approach to modulate brain function *Neurol. Res.* **33** 825–31
Shah A, Dutta J, Wyrsch N, Prasad K, Curtins H, Finger F, Howling A and Hollenstein C 1992 VHF plasma deposition: a comparative overview *MRS Online Proc. Libr.* **258** 15
Steel H, Brüningk S C, Box C, Oelfke U and Bartzsch S H 2021 Quantification of differential response of tumour and normal cells to microbeam radiation in the absence of FLASH effects *Cancers* **13** 3238
Stevenson A W, Crosbie J C, Hall C J, Häusermann D, Livingstone J and Lye J E 2017 Quantitative characterization of the x-ray beam at the Australian Synchrotron imaging and medical beamline (IMBL) *J. Synchrotron Radiat.* **24** 110–41
Trappetti V, Fazzari J M, Fernandez-Palomo C, Scheidegger M, Volarevic V, Martin O A and Djonov V G 2021 Microbeam radiotherapy—a novel therapeutic approach to overcome radioresistance and enhance anti-tumour response in melanoma *Int. J. Mol. Sci.* **22** 7755
Treibel F, Nguyen M, Ahmed M, Dombrowsky A, Wilkens J J, Combs S E, Schmid T E and Bartzsch S 2021 Establishment of microbeam radiation therapy at a small-animal irradiator *Int. J. Radiat. Oncol. Biol. Phys.* **109** 626–36
Wilson J D, Hammond E M, Higgins G S and Petersson K 2020 Ultra-high dose rate (flash) radiotherapy: silver bullet or fool's gold? *Front. Oncol.* **9** 1563
Wu X, Shu C, He X, Wang S, Fan X, Yu Z, Yan D and Huang W 2020 Optically transparent and thermal-stable polyimide films derived from a semi-aliphatic diamine: synthesis and properties *Macromol. Chem. Phys.* **221** 1900506